



Cite this: *Phys. Chem. Chem. Phys.*,  
2019, 21, 4375

# Molecular dynamics investigation of the influence of the shape of the cation on the structure and lubrication properties of ionic liquids†

Miljan Dašić, <sup>a</sup> Igor Stanković <sup>\*a</sup> and Konstantinos Gkagkas <sup>b</sup>

We present a theoretical study of the influence of the molecular geometry of the cation on the response of ionic liquids (ILs) to confinement and mechanical strain. The so-called tailed model includes a large spherical anion and asymmetric cation consisting of a charged head and a neutral tail. Despite its simplicity, this model recovers a wide range of structures seen in ILs: a simple cubic lattice for small tails, a liquid-like state for symmetric cation–tail dimers, and a molecular layer structure for dimers with large tails. A common feature of all investigated model ILs is the formation of a fixed (stable) layer of cations along solid plates. We observe a single anionic layer for small gap widths, a double anionic layer for intermediate ones, and tail-to-tail layer formation for wide gaps. The normal force evolution with gap size can be related to the layer formed inside the gap. The low hysteretic losses during the linear cyclic motion suggest the presence of strong slip inside the gap. In our model the specific friction is low and the friction force decreases with tail size.

Received 30th November 2018,  
Accepted 23rd January 2019

DOI: 10.1039/c8cp07364c

rsc.li/pccp

## 1 Introduction

Ionic liquids (ILs) are two-component systems composed of large asymmetric and irregularly shaped organic cations and anions. The feature of irregularity is important as it effectively prevents low-temperature ordering and crystallisation. Therefore, ILs are usually in the melted or glassy state. The physical properties of ILs like negligible vapour pressure, high-temperature stability, and high ionic conductivity and also a great variety of ILs and their mixtures highlight them as potentially relevant to lubrication.<sup>1,2</sup> A large number of variations in IL composition are possible, estimated at the order of magnitude of  $10^{18}$  different ILs.<sup>3</sup> From their variety stems the possibility of tuning their physicochemical properties which can affect lubrication such as viscosity, polarity, surface reactivity by varying their atomic composition, and the cation–anion combination. Hence, it would be advantageous if we could deduce general relations between the molecular structure and anti-wear and lubrication properties of ILs.

Since 2001, when ionic liquids were first considered for lubrication applications,<sup>4</sup> there has been a large number of experimental studies in that direction. It has been observed that

the alkyl chain length of the cations affects the IL's viscosity,<sup>1</sup> melting point<sup>1</sup> and pressure–viscosity coefficients.<sup>5</sup> Related specifically to lubrication, Dold *et al.*<sup>3</sup> and Minami<sup>6</sup> explored the impact of the cationic alkyl chain's length on the tribological properties of ILs. ILs considered in those references have the same cation but different anions (symmetric hexafluorophosphate  $[\text{PF}_6]^-$  and asymmetric bis(trifluoromethylsulfonyl)imide  $[\text{Tf}_2\text{N}]^-$ , respectively). Still, while Minami observed that the coefficient of friction (COF) decreases from 0.25 to 0.15 with the increase of alkyl chain length  $n_C = 2$  to 12 ( $n_C$  is the number of carbon atoms), Dold *et al.* observed that the COF increases from 0.025 to 0.1. The IL's wetting properties are also sensitive to its molecular geometry. ILs exhibit different wetting behaviours depending on the anion size:<sup>7–9</sup> from the absence of wetting to partial or complete wetting. A well-studied IL,  $[\text{BMIM}]^+[\text{PF}_6]^-$ , exhibits full wetting at the interface with mica substrates.<sup>7,8</sup> In contrast,  $[\text{BMIM}]^+[\text{TFSI}]^-$  shows partial wetting on mica.<sup>8,9</sup> In these examples, the ILs have the same cation and different anions.

An important observation about the structure of confined ILs is their arrangement into positively and negatively charged ionic layers and adsorption onto solid surfaces.<sup>10,11</sup> These ionic adsorption layers should reduce friction and prevent wear, especially in the case of boundary lubrication.<sup>10</sup> The wear is reduced primarily in two ways: *via* high load-carrying capability and self-healing of adsorbed IL layers. Still, these two processes seem conflicting with each other since high load-carrying capability requires strong adsorption of the lubricant to the surface, while self-healing requires high mobility.<sup>12</sup> Understanding the

<sup>a</sup> Scientific Computing Laboratory, Center for the Study of Complex Systems, Institute of Physics Belgrade, University of Belgrade, Pregrevica 118, 11080 Belgrade, Serbia. E-mail: igor.stankovic@ipb.ac.rs

<sup>b</sup> Advanced Technology Division, Toyota Motor Europe NV/SA, Technical Center, Hoge Wei 33B, 1930 Zaventem, Belgium

† Electronic supplementary information (ESI) available. See DOI: 10.1039/c8cp07364c

driving forces between them requires relating the molecular structure and flow properties of confined ILs. Kamimura *et al.*<sup>13</sup> evaluated the tribological properties of different ionic liquids using a pendulum and ball on disk tribo testers. They considered ILs consisting of imidazolium cations with different alkyl chain lengths and  $[\text{TF}_2\text{N}]^-$  anions as lubricants. Their main observation is that the increment of alkyl chain length can reduce the friction and wear of sliding pairs in the elastohydrodynamic lubrication (EHL) regime as a consequence of the increased viscosity. Generally, the conclusion is that longer alkyl chains lead to better tribological performance. Related to the impact of alkyl chain length on the structure of ILs, Perkin *et al.*<sup>14</sup> experimentally achieved the formation of tail-to-tail bilayers of cations when their alkyl chain length was large, in case of confinement between solid surfaces. Their observations are in accordance with other experimental investigations of IL lubricants.<sup>15–17</sup> In this work, we have obtained similar configurations *via* numerical simulations of ILs confined between two solid plates, where tail-to-tail formation in the middle of the interplate gap is visible.

In this theoretical study, we apply a coarse grained Molecular Dynamics (MD) simulation setup consisting of two solid plates and an IL placed between them. Our simulation setup also includes lateral reservoirs into which the IL can dynamically expand.<sup>18</sup> The focus of our study is on the systematic investigation of the flow properties and lubrication mechanisms of ionic liquids modelled with a generic coarse grained model which considers a variable shape of the cation. We investigate the impact of cationic tail size on the structural and tribological properties of ILs *via* molecular dynamics simulations. Such an idea is meaningful since previous theoretical studies have pointed out that confinement modifies the behaviour of ILs, and despite their good wetting nature, slip is present at the plates.<sup>19</sup> Coulombic interactions in ILs induce long-range ordering,<sup>19–21</sup> which in turn can influence their lubrication response. Recently, there have been substantial modelling efforts towards the investigation of ILs as lubricants.<sup>22–24</sup> Coarse grained approaches, being less computationally expensive, have an advantage for reaching the length- and time-scales that can be of relevance to the systems of industrial interest. Previously, coarse grained MD simulations<sup>25–31</sup> were used to study thin lubricant films subjected to shearing between solid plates.

We outline the content of this paper: the Model section describes the interactions taken into account and the MD simulation setup. The focus of the Bulk ionic liquids section is first on obtaining the relaxed structures and then on calculating the viscosity coefficients of bulk ionic liquids. In the following Confined ionic liquids section we present and discuss the static and dynamic behaviours of confined ionic liquids. This section also presents the results of the friction behaviour of confined ILs. We present the overview of contributions in the Discussion section followed by the Conclusion.

## 2 Model

In this study, we have applied a generic coarse grained IL model, introduced in ref. 24. In this model, the anion is represented as a

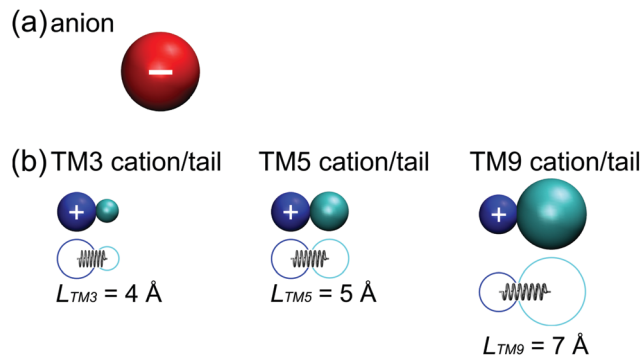


Fig. 1 Schematic representations of (a) anion and (b) cation molecules in a TM. The anion is represented by a spherical particle with a diameter  $\sigma_A = 10 \text{ \AA}$ . The cation molecule consists of a charged head with a diameter  $\sigma_C = 5 \text{ \AA}$  and a neutral tail. In order to be more concise, we refer just to the cationic head as the cation. The cation and its tail are connected using a spring with length  $L = (\sigma_C + \sigma_T)/2$ . The size of the tail has been varied and (a) TM3, (b) TM5 and (c) TM9 ionic liquids have tail diameters of 3, 5 and 9 Å, respectively. The molecular asymmetry is a feature of real ionic liquids and the chosen parameters resemble  $[\text{BMIM}]^+[\text{PF}_6]^-$  IL properties, cf. ref. 22 and 23.

negatively charged large-sized spherical particle, while the cation is a dimer consisting of a positively charged small-sized spherical particle (*i.e.* cationic head), and a neutral spherical particle (tail) attached to the corresponding cationic head *via* an elastic spring, see Fig. 1. Since the cationic tail is the principal feature of the model used in this paper, we will refer to it as a tail model (TM). The asymmetry of the cation leads to amorphous (glassy) states for realistic values of interaction parameters (*e.g.*, for hydrocarbons), in contrast to the simplest coarse-grained model of an IL known as a salt-like model (SM), where both cations and anions are spherical. The SM has already been exploited in previous studies.<sup>18,22,24,32</sup> Despite its obvious advantage of simplicity, in order to avoid crystallization, the SM relies on a very weak non-bonded Lennard-Jones interaction, which makes any comparison with real ILs only qualitative. In addition, the SM cannot account for molecular asymmetry featured in real ILs. Nevertheless, the SM has been proven to be quite useful for the development of the simulation methodology, as it reduces computational complexity and enables faster equilibration (*e.g.*, for obtaining static force–distance characteristics as in ref. 18). More complex extensions of TM coarse grained models can involve several tails of different sizes, like in ref. 22. For simplicity reasons, we restrict our considerations in this study to a single neutral tail of variable size. Although a whole cationic dimer is an entity which actually represents a cation, in order to be more concise we refer just to the cationic head as the cation.

### 2.1 Interaction model

In cation–tail dimers an elastic spring connects cations and neutral tails, enabling the tail's freedom of moving independently from its cation, since their connection is not rigid, cf. Fig. 1. Interatomic interactions taken into consideration in our MD simulations are: (i) non-bonded Lennard-Jones (LJ) and

Coulombic electrostatic interactions and (ii) bonded interaction (an elastic spring potential in cation–tail pairs):

$$V_{\alpha\beta}(r_{ij}) = 4\epsilon_{\alpha\beta} \left[ \left( \frac{\sigma_{\alpha\beta}}{r_{ij}} \right)^{12} - \left( \frac{\sigma_{\alpha\beta}}{r_{ij}} \right)^6 \right] + \frac{1}{4\pi\epsilon_0\epsilon_r} \frac{q_i q_j}{r_{ij}}, \quad (1)$$

where  $i, j = 1, \dots, N$  are particle indices, and  $N$  is the total number of particles. Particles can be of different types  $\alpha, \beta = A, C, T, P$ , which refer to anions, cations, tails, and solid plate atoms, respectively. Interaction of tails (*i.e.*, at least one of the indices  $\alpha, \beta = T$ ) with all other atom types, including tails themselves, is implemented using a purely repulsive potential. The ionic liquid is electro-neutral, *i.e.*, the numbers of cations and anions are the same. All MD simulations in this study were performed using the LAMMPS software.<sup>33</sup> More details are provided in the ESI.†

## 2.2 Model parameters

In this study we have fixed the diameters of the cationic heads and anions at  $\sigma_C = 5 \text{ \AA}$  and  $\sigma_A = 10 \text{ \AA}$ , respectively. Such a choice respects the asymmetry that exists in ILs and it is consistent with other models, as well as, for example, the [BMIM]<sup>+</sup>[PF<sub>6</sub>]<sup>−</sup> ionic liquid, *cf.* ref. 18 and 22–24. The solid plate atoms have a diameter of  $\sigma_P = 3 \text{ \AA}$ . We have taken into consideration three different tailed-models of the IL depending on the tail size, which is defined by its Lennard-Jones  $\sigma_T$  parameter: a small-tail cationic dimer (*i.e.*, TM3 with  $\sigma_T = 3 \text{ \AA}$ ), a symmetric cationic dimer (*i.e.*, TM5 with  $\sigma_T = \sigma_C = 5 \text{ \AA}$ ) and a large-tail cationic dimer (*i.e.*, TM9 with  $\sigma_T = 9 \text{ \AA}$ ), see Fig. 1. Drawing a comparison with the experiment in ref. 3 and 6, the TM IL mimics a folded alkyl chain and the radius of the sphere is related to the gyration radius of the chains. Depending on the length of the alkyl chain, the sphere has a smaller or larger radius. Thus, the size of a sphere which represents a neutral tail in TM ILs does not compare directly with the alkyl chain length. However, we can make a qualitative analogy. While the representation of the alkyl chain as a neutral LJ sphere does not include all the microscopic level features, we will show that the three selected radii, *i.e.*,  $\sigma_T = \{3, 5, 9\} \text{ \AA}$ , result in clear differences in the bulk properties of the ILs and their lubrication response.

Each cation–tail pair is connected *via* an elastic spring defined by the next two parameters: elastic constant  $K = 80 \text{ kcal mol}^{-1} \text{ \AA}^{-2}$  and equilibrium length of the spring  $L = (\sigma_C + \sigma_T)/2$ . To account for the dielectric screening, the dielectric constant is set to  $\epsilon_r = 2$  as in ref. 18, 23 and 24. The strength of the LJ interactions between different charged parts of ions ( $\alpha, \beta = A, C$ ) is  $\epsilon_{\alpha\beta} = 1.1 \text{ kcal mol}^{-1}$ . The LJ parameters are chosen to compare well with one of the most widely studied ionic liquids, [BMIM]<sup>+</sup>[PF<sub>6</sub>]<sup>−</sup>, *cf.* ref. 22 and 23. The charges of ions are set to elementary:  $q_C = +e$  and  $q_A = -e$ , where  $e = 1.6 \times 10^{-19} \text{ C}$ . The tails interact with all other particle types repulsively. The strength of the ion–substrate interaction was tuned to ensure complete wetting,  $\epsilon_{\alpha P} = 5.3 \text{ kcal mol}^{-1}$ , where  $\alpha = A, C, T$ .‡ All the values of the  $\{\epsilon_{\alpha\beta}, \sigma_{\alpha\beta}\}$  parameters used in our

‡ Only when the strength of the ion–substrate LJ interaction equals the strength of the inter-ionic LJ interaction, partial wetting is observed, *i.e.*,  $\epsilon_{\alpha P} = 1.1 \text{ kcal mol}^{-1}$ , as reported in the ESI.†

simulations are listed in the ESI.† The cross-interaction parameters are calculated using Lorentz–Berthelot mixing rules.

## 3 Bulk ionic liquids

### 3.1 Bulk structure

An initial configuration for a bulk ionic liquid was obtained by a random placement of ions ( $N_C = N_A = 1000$ ) into a cubic simulation box with periodic boundary conditions in all three directions. The simulation box volume was chosen to ensure that the resulting pressure after the relaxation of the IL structure is comparable to the one experienced by a thin confined IL film studied in the following section of this paper. In the case of the present system the pressure is  $p \approx 10 \text{ MPa}$ , which corresponds to a normal force of 1 nN acting on a surface of  $10^4 \text{ \AA}^2$ . Relaxation of the internal energy and pressure for the three TM ILs is presented in detail in the ESI.†

Fig. 2 presents the  $xy$  cross-sectional snapshots of bulk IL configurations at the end of relaxation simulations, again for (a) TM3, (b) TM5 and (c) TM9. These results have clearly revealed a strong dependence of the IL's structure on the tail size. It can be observed that (i) small tails in TM3 lead to cubic crystalline arrangement of ions, (ii) symmetric cationic dimers in TM5 enable a liquid-like state of the IL, and (iii) large tails in TM9 dictate ordering in the way that ions form layers with tails in-between.

These results are in agreement with experimental observations of the relationship between the length of the alkyl chain and the structure of a bulk IL.<sup>34</sup> When the cation alkyl chain is short, the Coulombic forces are dominant, enabling order. We observe this kind of result with TM3. Alkyl chains must be long enough in order to suppress the Coulombic interactions, *e.g.* the number of C atoms  $n_C \approx 12$ , which corresponds to the tail length of  $(n_C - 1) \cdot 1.53 \text{ \AA} = 16.83 \text{ \AA}$ , taking into account that a C–C bond has a length of 1.53 Å. The suppression of Coulombic interactions results in the absence of order, as we obtain with TM5, *cf.* Fig. 2(b). However, the tail should not be too large since large tails tend to arrange into a separate layer. This leads to a reappearance of layered structural ordering, like in the case of TM9, *cf.* Fig. 2(c). This layering can take place even when the cohesive interaction between the tails is absent, since in our TM IL the pair-interaction of tails with all other particles is repulsive.

### 3.2 Bulk IL viscosity characteristics

We have calculated the viscosity using non-equilibrium (NEMD) simulations of the three TM IL systems in a box with periodic boundary conditions in all three directions under different shear rates. Since in bulk simulations the whole simulation box is sheared, the shape of the box changes. Therefore, we use the so-called SLLD thermostat<sup>35,36</sup> (more details are provided in the ESI.†). For each value of  $\dot{\gamma}$  in the range  $0.01\text{--}10 \text{ ns}^{-1}$ , we have calculated the average shear stress from three stress tensor components:  $\tau = (\tau_{xy} + \tau_{xz} + \tau_{yz})/3$ . The average shear stress  $\tau$  and shear rate  $\dot{\gamma}$  are related by

$$\tau = \eta \cdot \dot{\gamma}^\alpha, \quad (2)$$

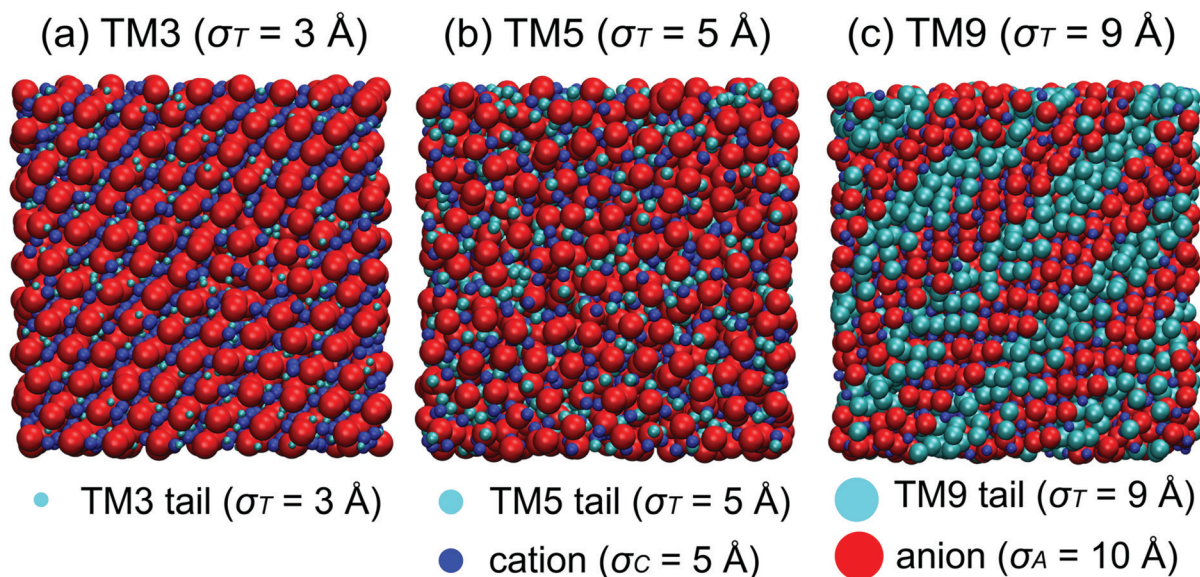


Fig. 2 Configuration snapshots of bulk (a) TM3, (b) TM5 and (c) TM9 ionic liquids, with tail diameters of 3, 5 and 9 Å, respectively. We may notice that each configuration snapshot represents a different state, *i.e.* the TM3 bulk IL crystallizes into a tilted simple cubic crystal structure, oriented along the face diagonal; the TM5 bulk IL is in a liquid state; the TM9 bulk IL crystallizes into crystal planes with alternating ionic-tail layers, oriented along the face diagonal as well.

where  $\eta$  is the generalised viscosity coefficient and  $\alpha$  is an exponent. In addition to the NEMD method of simulation box shearing, we have also calculated the zero shear rate viscosity  $\eta^{\text{GK}}$  using the Green–Kubo (GK) relation for the three model ILs, as the integral of the stress tensor auto-correlation functions, see ref. 37 and 38.

In Fig. 3 we present the dependence of the average shear stress  $\tau$  on the shear rate  $\dot{\gamma}$  for the TM3, TM5 and TM9 bulk ILs. We notice that the average shear stress remains within the same order of magnitude in the TM3 and TM9 systems, although the shear rate changes by four orders of magnitude. As a result, the corresponding values of the exponent  $\alpha$  are low, *i.e.*  $\alpha_{\text{TM3}} = 0.15 \pm 0.02$  and  $\alpha_{\text{TM9}} = 0.12 \pm 0.04$ . The bulk ILs in

the case of TM3 and TM9 are ordered. The presence of order results also in high values of their Green–Kubo viscosities, *i.e.*  $\eta_{\text{TM3}}^{\text{GK}} = 4.72$  mPa s and  $\eta_{\text{TM9}}^{\text{GK}} = 1.67$  mPa s. In contrast to that, we observe a more than two orders of magnitude change in the average stress tensor component in the case of symmetric cations and a liquid-like bulk structure (TM5). We have obtained  $\alpha_{\text{TM5}} = 0.8 \pm 0.1$ , which is relatively close to a Newtonian viscous fluid, *i.e.*,  $\alpha = 1$ . The viscosities determined *via* shearing simulations and *via* the GK relation in the case of TM5 are different; however, they are of the same order of magnitude:  $\eta_{\text{TM5}} = 0.1435$  mPa s and  $\eta_{\text{TM5}}^{\text{GK}} = 0.6144$  mPa s.

## 4 Confined ionic liquids

For the study of ILs under confinement, we use the MD simulation setup of ILs under confinement shown in Fig. 4. The ionic liquid is placed between two solid plates: a bottom plate which is continuous in two dimensions (in the  $xy$ -plane) and a top plate which is infinite in one dimension (along the  $x$ -axis) and features lateral reservoirs in the other, *i.e.*, along the  $y$ -axis. This design allows long-range ordering of the ILs on the surface while at the same time creating quasi-micro-canonical conditions inside the interplate gap. We use this setup throughout the paper in order to investigate both the static and dynamic behaviours of the confined IL, as well as its lubrication performance. We keep the simulation setup geometry fixed, and we change the IL. Additional implementation details can be found in the ESI.†

### 4.1 Equilibrium behaviour of confined ionic liquids

Confinement induces layering in IL thin films.<sup>18,39</sup> In order to understand how an interplay between layering and the

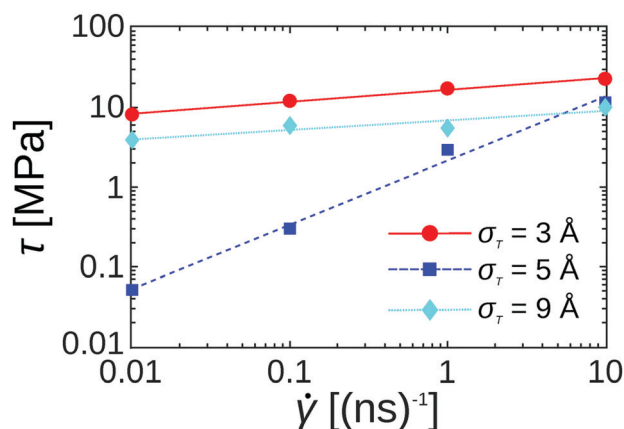


Fig. 3 Average shear stress  $\tau$  as a function of shear rate  $\dot{\gamma}$  of the TM3, TM5 and TM9 bulk ILs. We have conducted shear simulations for the shear rates in a range of four orders of magnitude ( $\dot{\gamma} = 0.01$ – $10$  ns<sup>-1</sup>). The lines are obtained by fitting the points with eqn (2).

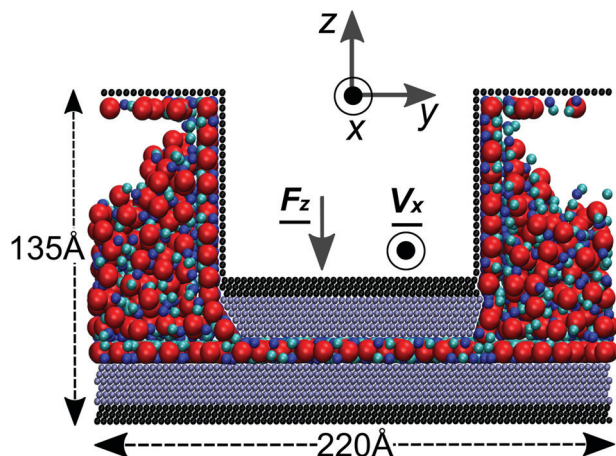


Fig. 4 Schematic of the simulation setup shown as a  $yz$  cross-section. The dimensions of the system along the  $y$  and  $z$  axes, together with the directions of the imposed normal load  $F_z$  and lateral velocity  $V_x$ , are noted. The total system length in the  $x$  direction is 125 Å. There are two solid plates at the top and bottom of the system (more details on the simulation configuration are given in the ESI<sup>†</sup>). The different regions have different colours. The ionic liquid is composed of equal numbers of cation–tail pairs and anions (particles can be visually distinguished: cations – blue spheres, tails – cyan spheres, and anions – red spheres).

molecular geometry of ILs alters the load bearing capability of the thin films, we calculate the quasi-static force–distance characteristics. We follow the evolution of the normal load  $F_z$  acting on the top plate as a function of interplate distance  $d_z$ . To ensure static conditions, the interplate distance is changed through a series of alternating steps, called move and stay, related to the movement of the top plate and subsequent relaxation of the IL structure, respectively. We describe in detail the simulation procedure in the ESI.<sup>†</sup> The results for the force–distance characteristics of the three TM ILs are presented in Fig. 5, where three different markers correspond to the three IL models. The normal force  $F_z$  strongly and non-monotonically depends on the distance  $d_z$ . These changes in the normal force  $F_z$  are correlated with the squeezing in and out of cation/anion layer pairs into the gap, as already observed experimentally<sup>40</sup> and theoretically.<sup>18</sup> The normal force becomes negative ( $F_z < 0$ ) only in the case of small tails (TM3). The negative values are a result of the IL trying to reduce the plate-to-plate distance due to the adhesion forces inside the IL. The increasing tail size seems to reduce the effect of adhesion: for large tails (TM9) the normal force at the minimum is close to zero, while for symmetric cation molecules (TM5) it becomes positive ( $F_z = 2$  pN).

For all three curves corresponding to the three TM ILs we can identify three characteristic ranges of the plate-to-plate distance  $d_z$ : the initial segment ( $11 \text{ Å} \leq d_z \leq 13.8 \text{ Å}$ ) characterized by a monotonic and steep decrease of the normal force  $F_z$ ; interval I ( $13.8 \text{ Å} \leq d_z \leq 19.8 \text{ Å}$ ) characterized by the presence of local minima and maxima peaks of the normal force  $F_z$ , and interval II and beyond ( $d_z \geq 19.8 \text{ Å}$ ) characterized by a continuous and gentle decrease of the normal force  $F_z$ , where in all three cases the normal force practically becomes zero when  $d_z > 32 \text{ Å}$ .

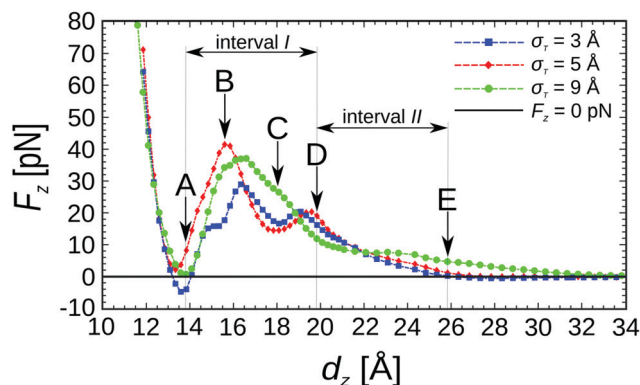


Fig. 5 Dependence of normal force  $F_z$  on plate-to-plate distance  $d_z$ . Five characteristic points denoted {A, B, C, D, E} with the corresponding interplate distances  $d_z = 13.8, 15.5, 18.0, 19.8,$  and  $25.8 \text{ Å}$ , respectively, are marked in the figure. They are chosen in the way that: point A is located in the proximity of a local minimum for all three cases; point B corresponds to a local maximum for TM5; point C is located in the proximity of a local minimum for TM3 and TM5; point D is located in the proximity of a local maximum for TM3 and TM5; and point E is chosen according to the condition  $\overline{DE} = \overline{AD}$ . For reference, the black horizontal line denotes  $F_z = 0$ . The lines connecting points (averages of normal force) serve as visual guides.

We will briefly describe the segments of the  $F_z(d_z)$  curves, pointing out similarities and differences between the different IL models. In the initial segment, *i.e.*, for small gaps  $d_z < 13 \text{ Å}$ , the normal force  $F_z$  is practically the same for all three systems, meaning that it does not depend on the tail size. The steep increase of the normal force with compression in the range  $d_z < 13 \text{ Å}$  is a sign of a very high resistance of the single anionic layer left in the gap to squeeze out. On the other hand, at large gap values (*i.e.*,  $d_z > 32 \text{ Å}$ ), the normal loads  $F_z$  in all three TM ILs are similar and small. We can conclude that at large gaps there is a low resistance of the IL to the gap changes. Significant differences in the force–distance curves depending on the tail size exist only in interval I, *i.e.*,  $13.8 \text{ Å} \leq d_z \leq 19.8 \text{ Å}$ . In the case of TM3, the  $F_z(d_z)$  characteristic curve has two local minima and maxima and one saddle point; in TM5 there are two local minima and maxima; and for TM9, there is one local minimum and maximum.

**4.1.1 IL layer structure inside the gap.** In Fig. 6 we show the ionic density distribution along the  $z$  axis for the three IL models, at points A to E, *i.e.*,  $d_z = \{13.8, 15.5, 18.0, 19.8, 25.8\} \text{ Å}$ . A common feature of all investigated IL models is the formation of fixed cationic layers along the whole length of the solid plates (top and bottom). The fixed layers and their stability are a result of strong LJ interactions between the plates and ions. In general, the smallest particles form the first layer next to the plates: for TM3 these particles are tail particles (which are part of the cation–tail pair), while for TM5 and TM9 these particles are the cations. The consecutive layers are formed inside the interplate gap *via* combined volume exclusion and Coulombic interactions, and their ordering is consistent with the fixed layers. As a result, tails migrate to the plates in TM3, mix with the cationic layer when the cation–tail dimer is symmetric in TM5, and finally mix into the anionic layer when they are large in TM9.

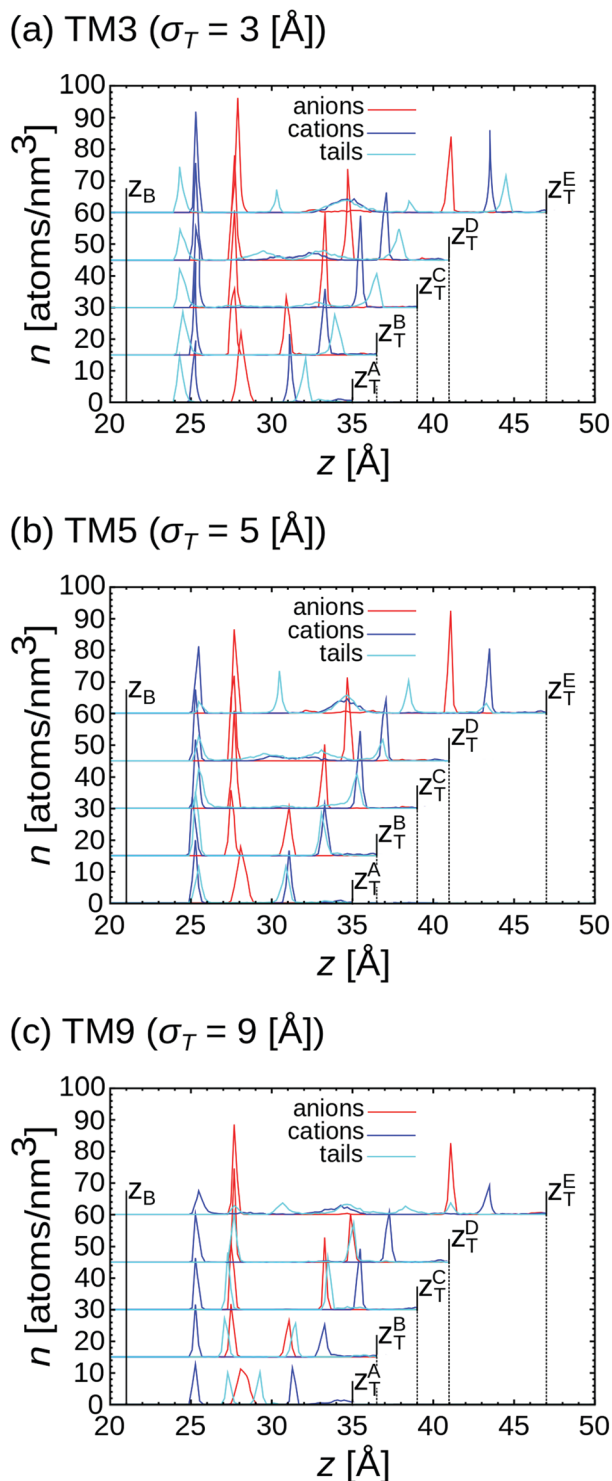


Fig. 6 Ionic density distribution of ions inside the interplate gap of (a) TM3, (b) TM5 and (c) TM9 in characteristic points {A, B, C, D, E} selected in the static force–distance characteristics presented in Fig. 5. The positions of the atomic centres of the innermost atomic layers of the (moving) top and (fixed) bottom plates are labeled  $z_T^{A-E}$  and  $z_B$ , respectively. The five characteristic points, denoted {A, B, C, D, E}, have the corresponding interplate distances  $d_z = z_T - z_B = 13.8, 15.5, 18.0, 19.8,$  and  $25.8$  Å, respectively.

Since Coulombic interactions cause the layering with alternating charge signs, layers of anions always separate the cation layers.

We focus on analysing the changes in the segment between points A and D, *i.e.*, interval I. The normal force  $F_z$  changes rapidly and non-monotonically with  $d_z$  in interval I, *cf.* Fig. 5. For the minimum of  $F_z$  in the vicinity of point A, *i.e.*, for plate-to-plate distance  $d_z^A = 13.8$  Å, we can observe a well-defined anionic layer in Fig. 6 (the corresponding snapshots of configurations are given in the ESI†). The most interesting change takes place during the A  $\rightarrow$  B transition when the single layer of anions is split into two layers, *cf.* Fig. 6. As a result, the normal force  $F_z$  increases and reaches a local maximum in the proximity of point B, *i.e.*, for plate-to-plate distance  $d_z^B = 15.5$  Å. We observe that additional anion–cation pairs are pulled inside the gap in Fig. 7. We also observe that the two anionic layers in Fig. 6 for point B and the one for point A have the same maximum number density. As we increase  $d_z$  further, the number of anionic layers confined inside the gap remains unchanged and the normal load  $F_z$  decreases slowly. At the same time, the number of ions inside the gap steadily increases with gap width. Nevertheless, this increase is not sufficient to keep the density of the IL inside the gap constant (*cf.* Fig. 7). Looking into the changes in the spatial distribution of the IL components, as more cation–anion pairs are pulled into the gap (going from A  $\rightarrow$  E), we observe a steady increase of the concentration of anions in the layer next to the bottom plate. In the case of TM5 we have an increase from  $n_{TM5}^A = 18$  atoms per  $\text{nm}^3$  to  $n_{TM5}^D = 27$  atoms per  $\text{nm}^3$ , *cf.* Fig. 6. When we further look at configuration snapshots for TM3 and TM5, a formation of additional layers inside the gap is visible, between points C and D. This can also be clearly observed in Fig. 6 and results in a smaller maximum around  $d_z = 19$  Å, in Fig. 5. We can conclude that the normal force–plate distance characteristics are not correlated with the number density of the IL molecules inside the gap, but with the layer formation as seen in Fig. 6.

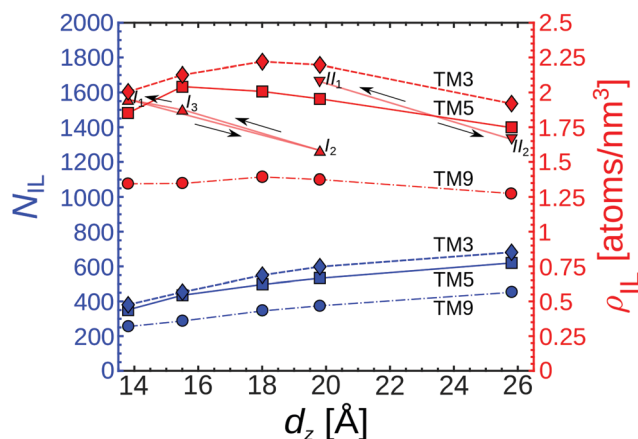


Fig. 7 Evolution of the number of confined ionic liquid (IL) molecules (bottom curves) and density (top curves) inside the gap with gap width  $d_z$  for TM3, TM5 and TM9 at characteristic points {A, B, C, D, E} selected from the static force–distance characteristics (Fig. 5). The corresponding axes for the number of IL molecules and the density are given on the left and right sides, respectively. The densities at characteristic points for the dynamic cases (intervals I and II) are also given, *i.e.*,  $I_{1,2,3}$  and  $II_{1,2}$ . The five characteristic points denoted {A, B, C, D, E} in the static and  $I_{1,2,3}$  and  $II_{1,2}$  dynamic cases have the same corresponding interplate distances  $d_z = 13.8, 15.5, 18.0, 19.8,$  and  $25.8$  Å, respectively.

As the interplate distance  $d_z$  increases further, from point D to E, we notice additional cations in the middle of the gap and the formation of a third cationic layer in all three systems. We can make an interesting observation: for all three models the tails in the middle of the confinement are grouped into three regions: one overlapping with cations at  $z = 34$  Å and two located between the cationic and anionic layers, *i.e.*,  $z = 30$  and  $38$  Å, *cf.* in Fig. 6. This outcome is reminiscent of the findings from ref. 14, where the authors have experimentally obtained the formation of the tail-to-tail bilayer of cationic dimers in case the alkyl chain length is oversized.

**4.1.2 IL crystallinity: the influence of the gap.** We show the  $xy$  cross-sectional snapshots in Fig. 8 in order to observe the IL's in-plane structure at the cross-section just below the top plate. We mark the boundaries of the top plate spatial region with the vertical dashed lines. The central area of the panels in the figure corresponds to the interplate gap region and it represents a half of the total cross-section's width in the  $y$  direction, while the remaining area corresponds to the lateral reservoirs. The solid lines mark the orientation of crystal grains in those areas, where we can observe the presence of structural ordering. In the case of TM3, we observe the presence of partial triangular ordering only at point B when the structure is the most compressed. We do not notice any crystallization for symmetric

dimers (TM5), which confirms that the symmetric tail prevents ordering both under confinement and in the bulk. Contrary to the previous two cases, we observe crystallization for all configurations with the large tail (TM9). Additionally, we observe changes in the type of crystalline structure. While in the lateral reservoirs a triangular lattice arrangement is always present, depending on the amount of compression we observe triangular lattice arrangements at points A and D and square lattice arrangements at points B and C. Even more surprisingly, the order is lost when the tail-to-tail bilayer is formed at point E.

## 4.2 Cyclic extension and compression of confined ILs

The top plate was moved between the two limiting points of intervals I ( $d_z^A \leq d_z \leq d_z^D$ ) and II ( $d_z^D \leq d_z \leq d_z^E$ ). We investigated the dynamic behaviour of the confined IL thin film during the cyclic movement of the top plate along the  $z$  axis, *i.e.*, the interplate gap was periodically extended (extension half-cycle) and compressed (compression half-cycle). We investigated our system at three velocities  $V_z = \{0.1, 1, 10\}$  m s<sup>-1</sup>, but we did not observe any velocity dependent differences in the system behaviour. The confined ionic liquid lubricant responds to the cyclic movement of the top plate with a hysteresis in normal force  $F_z(d_z)$  shown in Fig. 9. We present the detailed results of TM5's dynamic behaviour in panels (a) and (c) of Fig. 9. Also, in panels (b) and (d) of the same figure, we present together the smooth average cycles of our three IL models (TM3, TM5, and TM9).

**4.2.1 Narrow gap: normal force hysteresis.** We will now discuss in detail the response of TM5 to the cyclic motion of the top plate, in interval I shown in Fig. 9(a). Ten compression-extension cycles are shown (thin lines) with an average cycle superimposed on them (thick line). We identify three points of interest:  $\{I_1, I_2, I_3\}$ , *i.e.*, the two terminal points of the cycle and the point with the maximal normal force, respectively. These three points also correspond to points  $\{A, D, B\}$ , respectively, in the quasi-static characteristics shown in Fig. 5. Point  $I_3$  corresponds to the maximum of normal force  $F_z$  both in the cyclic compression cycle and in the static characteristics of TM5, which makes the comparison more straightforward.

The normal force  $F_z$  decreases down to a value close to zero during the extension half of the  $I_1 \rightarrow I_2$  cycle. The anion-cation pairs are pulled into the gap from the lateral reservoirs as the gap is extended and at point  $I_2$  an additional anionic layer is fully formed inside the gap. Actually, instead of the two fixed layers of cations which shared one anionic layer, we obtain two separate anionic layers. The total number of ions pulled in is about 60 atoms or 0.22 atoms per (nm<sup>2</sup> ns) at 1 m s<sup>-1</sup> plate linear speed. In the first part of the compression half-cycle,  $I_2 \rightarrow I_3$ , the ions are compressed and the density and the normal force  $F_z$  increase. Somewhat surprisingly, we observe that an equal number of ions flow out, while the normal force increases, *i.e.*,  $I_2 \rightarrow I_3$  and during its sharp decrease,  $I_3 \rightarrow I_1$  (*cf.* Fig. 7). The sharp decrease of the normal force  $F_z$  in the  $I_3 \rightarrow I_1$  segment is therefore a result of two processes: out-flow of the ions from the gap and the collapse of the anionic double layer and its rearrangement into a single anionic layer. The resulting

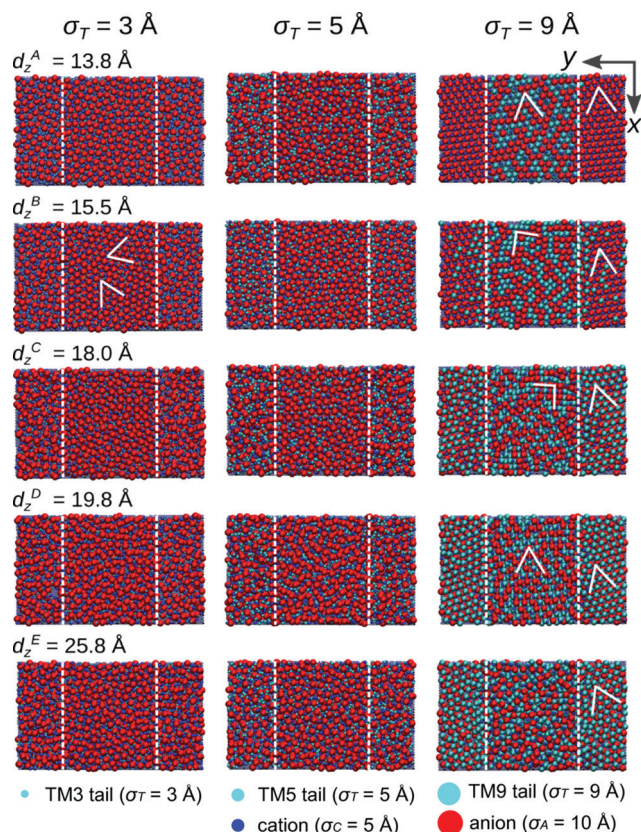


Fig. 8 Configuration snapshots ( $xy$  cross section) of TM3, TM5 and TM9 at five characteristic points  $\{A, B, C, D, E\}$ . The five characteristic points, denoted  $\{A, B, C, D, E\}$ , have the corresponding interplate distances  $d_z = 13.8, 15.5, 18.0, 19.8,$  and  $25.8$  Å, respectively (see also Fig. 5).

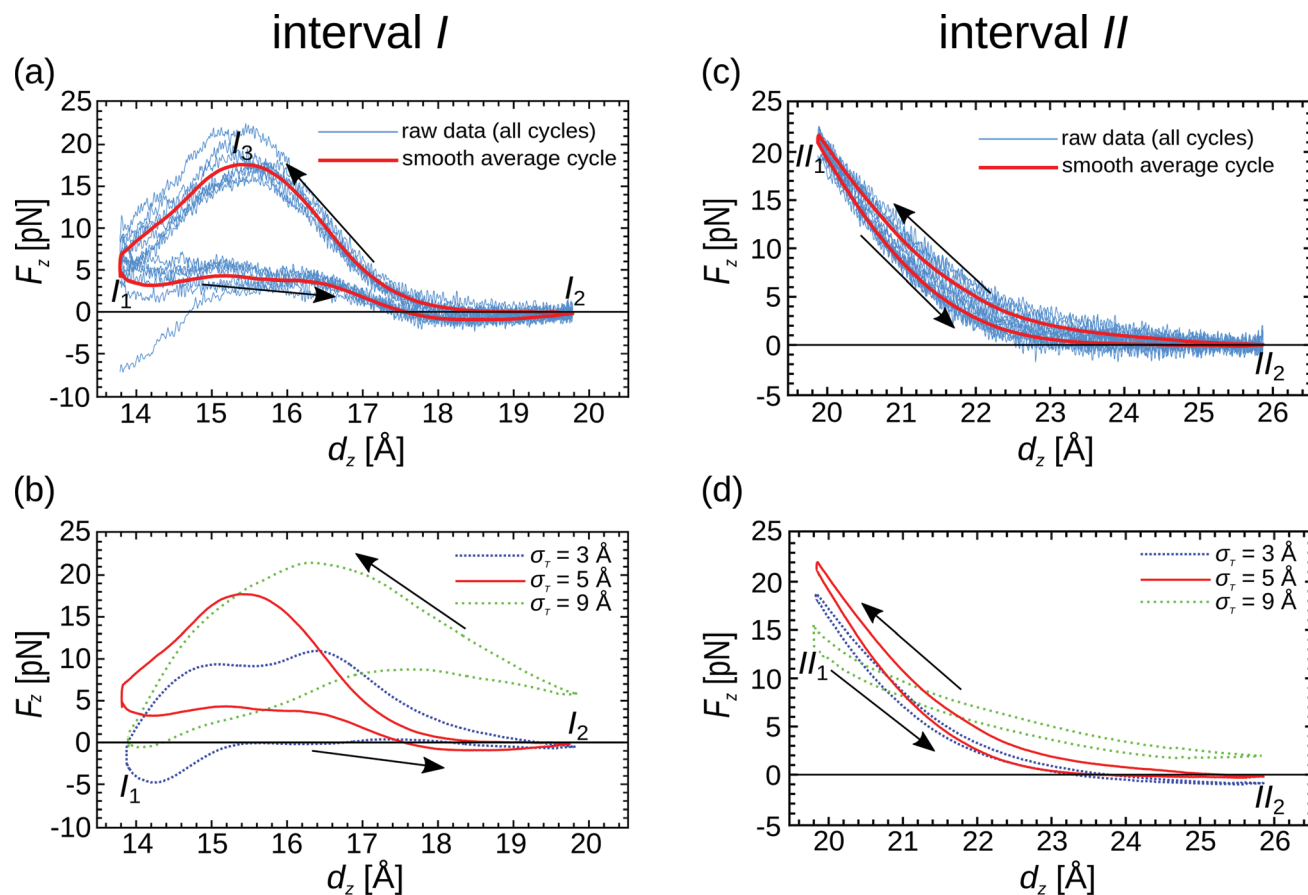


Fig. 9 The results of dynamic extension–compression cycles are shown for intervals I and II. In panels (a) and (c) we present dynamic  $F_z(d_z)$  characteristics in the case of TM5 for intervals I and II, respectively; thin lines represent the hystereses of ten dynamic cycles, and the solid line on top of them is the smooth average hysteresis. There is also a solid horizontal line which corresponds to  $F_z = 0$ . In (a) points  $I_1$ ,  $I_2$ , and  $I_3$  denote representative points:  $I_1$  – starting point,  $I_2$  – ending point,  $I_3$  – global maximum of the  $F_z(d_z)$  curve. In (c) points  $II_1$  and  $II_2$  denote representative points:  $II_1$  – starting point and  $II_2$  – ending point. The arrows show the direction of hysteresis (extension  $I/II_1 \rightarrow I/II_2$  followed by compression  $I/II_2 \rightarrow I/II_1$ ). In panels (b) and (d) we show together the smooth average hystereses  $F_z(d_z)$  of our three TMs, for intervals I and II, respectively. The starting and ending points and arrows are denoted, analogous to panels (a) and (c).

final density  $\rho_{\text{IL}}^{\text{dyn}} = 1.95$  atoms per  $\text{nm}^3$  of the system is slightly higher than in the static case  $\rho_{\text{IL}}^{\text{stat}} = 1.85$  atoms per  $\text{nm}^3$ , cf. Fig. 7. The value of the normal force  $F_z$  at point  $I_1$  is similar, i.e.,  $F_z = 4$  pN, in both the static and dynamic cases.

In Fig. 9(b), we observe that each one of the three investigated ionic liquids (TM3, TM5, and TM9) exhibits different behaviour in the average  $F_z(d_z)$  cycle during the extension and compression half-cycles. First, at the onset of the extension half-cycle, i.e. at point  $I_1$ , the normal force  $F_z$  has a positive value for symmetric cations (TM5), it is close to zero for large tails (TM9), and it is negative for small tails (TM3). Somewhat surprisingly, the normal force increases for both TM ILs with asymmetric cations (TM3/TM9), while it decreases for symmetric cations (TM5). The reason for this behaviour is the strong interaction of the fixed layers of ions adjacent to the plates with the plate particles. This interaction drives as many ions inside the gap as possible, resulting in the non-intuitive behaviour of the normal force due to the interplay of density and intra-IL LJ interactions. During the compression half-cycle for all three ILs the maximal normal force sustained was about

50% smaller than that in the quasi-static case, i.e., for TM5 the maximal force is  $F_z^{\text{max}} = 17$  pN in the dynamic case and  $F_z^{\text{max}} = 40$  pN in the static case (see Fig. 5 and 9(b)). This observation indicates that the top plate's motion prevents the IL from filling the gap. We can also conclude that the mechanical response is mainly due to the rearrangement of the fixed layer and that the mobility of the IL molecules is too low to significantly increase the normal force resisting the compression. If we analyse the rate of mass transfer outside of the gap, we conclude that there is a substantial slip, which results in a lower normal force. Without slip at a velocity  $V_z = 1$  m  $\text{s}^{-1}$ , the normal force calculated based on the bulk viscosity coefficient would be roughly two orders of magnitude higher.

**4.2.2 Wide gap: monotonic force–distance characteristics.** The expansion–compression force–inter-plate distance characteristics for interval II in the case of TM5 are given in Fig. 9(c). The difference from the quasi-static extension/compression in Fig. 5 is the monotonic behaviour during the strike. The quasi-static characteristics in interval II featured local minima and maxima in the case of TM3 and TM5. In the dynamic case, there are only

two characteristic points (starting and ending points)  $\{II_1, II_2\}$  and a monotonically changing normal force between them. In the extension half-cycle there is a continuous decrease of the normal force  $F_z$  followed by its continuous increase in the compression half-cycle. The difference between the cycles in the normal force is small. In the dynamic characteristics of interval II the layer structure is similar to that of the static case, *i.e.*, two fixed layers stay-in-place and the tail double layer is formed during the extension half-cycle (the configuration snapshots are given in the ESI†). In contrast to interval I, the formation of the additional layer of tails is not a result of the ions flowing from the lateral reservoirs into the gap. The density inside the gap is 10% higher in the dynamic case and a few atoms (less than 30) are displaced during the cycle. We should note that the gap is also 50% larger in interval I compared to interval II; therefore, the decrease in density is even less striking. Actually, the cyclic motion has a tendency to increase the density inside the gap. Since there is no large displacement of the ions in and out of the gap in interval II, there is also no maximum of the normal force  $F_z$ , similar to the one we have seen in the case of interval I, *cf.* Fig. 9(a). In order to make comparisons of different TM ionic liquid models, in Fig. 9(d) we show together the  $F_z(d_z)$  average cycle dynamic characteristics of all three IL models (TM3, TM5, TM9) for interval II. Compared to interval I, the tail size does not have such a pronounced impact on  $F_z(d_z)$  hysteresis curves in interval II.

#### 4.2.3 Energy losses due to cyclic expansion–compression.

At this point, we would like to quantify how the processes arising during the dynamic cyclic movement of the top plate contribute to energy losses. We calculate the area covered during the extension–compression cycle (*i.e.*, the area inside the  $F_z(d_z)$  hysteresis). This area is equivalent to the work invested per average dynamic cycle, *i.e.*, the hysteretic energy losses. We show the dependence of the energy losses on the tail size for both intervals I and II in Fig. 10. We observe a clear tendency of the increase of the invested work per dynamic cycle, with the increase of the tail diameter. This is primarily due to the larger volume occupied by the tails, resulting in larger normal forces

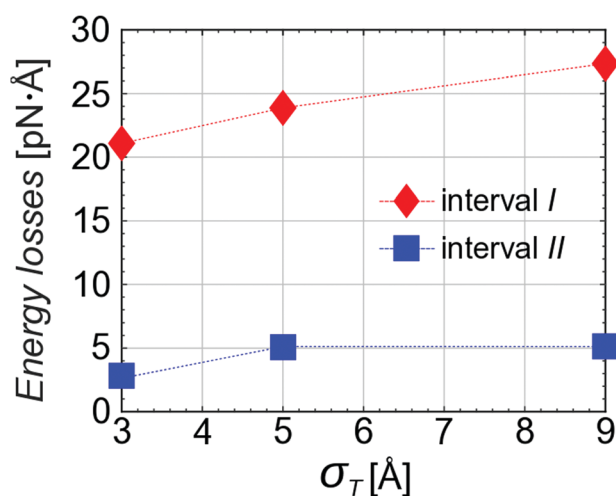


Fig. 10 Energy losses per average cycle as a function of the tail size for intervals I and II of dynamic extension–compression cycles.

resisting compression. There is a striking difference in the amount of invested work between the two intervals I and II (*e.g.* 27 pN Å for interval I of TM9 compared to 5 pN Å for interval II of TM9). This difference is proportional to the maximal normal force, which is sustained by the systems in the two intervals (*cf.* Fig. 5).

#### 4.3 Tribological behaviour of confined ionic liquids

We have conducted static and dynamic characteristic analysis of the three generic IL models, focusing on the influence of their molecular structure on their anti-wear performance. In order to obtain a full picture, it is crucial to determine the IL's friction behaviour under different shear conditions. In this section we apply a relative motion between the plates by moving the top plate along the  $x$ -axis (see Fig. 4) and we observe the resulting frictional force (also along the  $x$ -axis, *i.e.*,  $F_x$ ). We have performed two types of friction simulations: (i) at a constant top plate's velocity  $V_x = 2 \text{ m s}^{-1}$ , the simulations are performed at different fixed values of the gap:  $d_z = 12 \text{ Å}$  to  $25.5 \text{ Å}$ ; and (ii) at a fixed gap  $d_z = 15 \text{ Å}$  the top plate's lateral velocity takes five different values:  $V_x = \{0.1, 0.3, 1.0, 3.0, 10.0\} \text{ m s}^{-1}$ . In all friction simulations, the total distance covered by the top plate was  $\Delta_x = 100 \text{ Å}$  in the  $x$  direction.

The dependence of the time-averaged frictional force  $\langle F_x \rangle$  on the interplate gap  $d_z$  for the three IL models is shown in Fig. 11. The points obtained in the simulations are shown as markers. Linear fits through these points are provided as visual guides. For TM3, we observe a decrease of the frictional force  $\langle F_x \rangle$  with the size of the gap. On the other hand, the frictional force weakly depends on the interplate gap width in the case of TM5 and TM9 ILs. Both the TM3 and TM9 ILs have high zero shear-rate (Green–Kubo) bulk viscosities correlated with the extent of their ordering, *i.e.*,  $\eta_{\text{TM3}}^{\text{GK}} > \eta_{\text{TM9}}^{\text{GK}} > \eta_{\text{TM5}}^{\text{GK}}$ . When comparing their

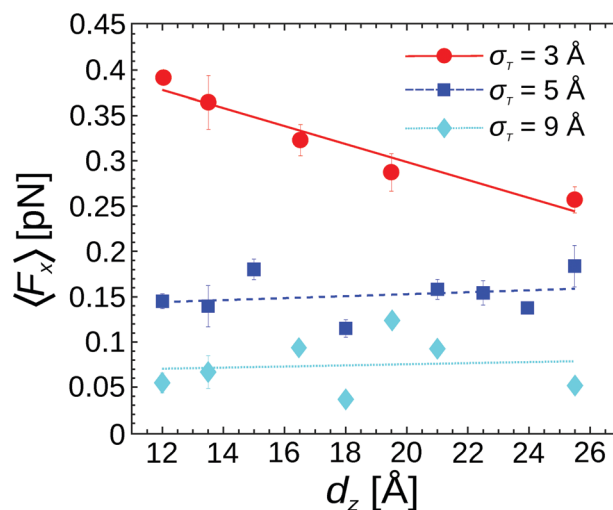


Fig. 11 Average frictional force  $\langle F_x \rangle$  acting on the top plate as a function of the plate-to-plate distance  $d_z$  for confined TM3, TM5 and TM9 ionic liquid lubricants. In the case of TM3 there is a clear linear dependence showing the decrease of frictional force intensity with gap increase, while in the case of TM5 and TM9 the frictional force is practically constant and does not depend on the gap.

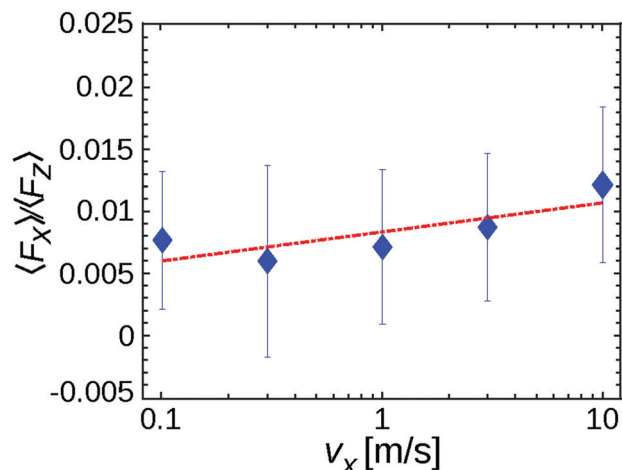


Fig. 12 Specific friction  $\frac{\langle F_x \rangle}{\langle F_z \rangle}$  dependence on the top plate's lateral velocity  $v_x$  in the case of TM5.

tribological performances in a thin film, we can conclude that there is no correlation since the TM5 IL has the highest average frictional force. In Fig. 12, we show the dependence of the specific friction  $\langle F_x \rangle / \langle F_z \rangle$  on the top plate's lateral velocity  $v_x$  in the case of TM5. We obtain specific friction values of the order  $\langle F_x \rangle / \langle F_z \rangle \approx 0.01$ , which are comparable to the results of Dold *et al.*<sup>3</sup> for symmetric  $[\text{PF}_6]^-$  anions. We also observe a similar tendency of decreasing friction force with respect to tail size, as reported in the same ref. 3.

The specific friction  $\langle F_x \rangle / \langle F_z \rangle$  is defined as the ratio of the time averaged frictional  $\langle F_x \rangle$  to normal  $\langle F_z \rangle$  force and it is different from the Coulombic friction coefficient  $\mu = \partial F_x / \partial F_z$ . Consistently with our previous results for model ionic liquids, we have observed a logarithmic dependence of the specific friction on the lateral velocity, *cf.* ref. 18. The numerical values are fitted to a linear function of the form  $\langle F_x \rangle / \langle F_z \rangle = a \log(v_x / v_{\text{ref}}) + b$ , where  $v_{\text{ref}} = 1 \text{ m s}^{-1}$ . The coefficients of the linear fit took the following values:  $a = 0.001$  and  $b = 0.008$ . A reasonable fit to the linear regression curve can be observed. The logarithmic dependence indicates typical elastohydrodynamic lubrication (EHL) conditions.<sup>41</sup>

## 5 Discussion

Ionic liquids interact *via* long-ranged Coulombic forces and their models require high-performance computational resources. This opens a question of the minimal model needed to capture the properties of the molecular processes governing lubrication mechanisms and the macroscopic performance relevant for engineering applications. In this paper, we investigate a generic tailed-model (TM) of ionic liquids (ILs), which includes an asymmetric cation consisting of a positively charged head and a neutral tail of variable size and a large spherical negatively charged anion. We observe that, though simple, this model results in striking differences in the equilibrium IL bulk structure governed by the tail size relative to the cationic head: (i) a simple cubic lattice for small tails, (ii) a liquid-like state for

symmetric cation–tail dimers, and (iii) a molecular layer structure for large tails.

We have investigated the influence of the molecular structure of a cation dimer on the response of three ILs to confinement and mechanical strain using molecular dynamics simulations. The properties of the three IL models are compared in and out of equilibrium. We have related the evolution of the normal force with inter-plate distance to the changes in the number and structure of the confined IL layers. We find that the density inside the gap has a secondary effect on the evolution of the normal force. We observe that symmetric molecules offset intra-IL adhesion due to the ordering of the IL. As a result, the thin layer of symmetric IL molecules exhibits non-negative normal force independent of the gap width. In analogy to the experimental observations, a tail-to-tail bilayer is formed for wide gaps in all three investigated model ILs. A mutual feature of all the investigated model ILs is the formation of fixed (stable) layers of cations along the solid plates. The fixed layer formation is a result of strong LJ interaction between the plates and ions. A consequence of the fixed layer stability is a steep increase of the normal force at small interplate gaps. The steep increase of the normal force is an effect useful for preventing solid–solid contact and the accompanying wear. The tails attached to the cations in the fixed layer migrate with increasing tail size. Small tails form the first layer next to the plates. For symmetric molecules the tails form a mixed layer with cations, while large tails form a mixed layer with anions.

We have explored the dynamic behaviour of IL thin films under cyclic extension–compression movements of the top plate. Two intervals of the interplate distances are investigated: a narrow gap interval, where the anionic layer is split into two, and a wide gap interval, where a tail-to-tail layer is formed. For the narrow gap interval, we observe a significant flow of ions during the cyclic motion of the top plate. A sharp decrease of the normal force at the final stage of compression is not only a consequence of the density change due to the flow, but is also a result of merging of the two anionic layers that repel each other by the electrostatic Coulomb forces into a single one. The mobility of ions in/out of the gap is driven by their interaction with plates, *i.e.*, filling of the fixed layers. As a result, for the narrow gap, the number of ions that entered the gap is 50% smaller in the dynamic case than in the static case. This results in a smaller density inside the moving narrow gap. The difference between the dynamic and static cases for the wide gap was even more striking. The number of ions that entered the gap is 80% smaller in the dynamic case than in the static case. Surprisingly, in the wide gap the density is higher in the dynamic case due to the lack of mobility of ions. The invested work per average cycle increases with tail size for all three IL models. As one could expect, the invested work is higher for the narrow gap where the number of confined ions/ionic layers changes during the cycle. Nevertheless, the low hysteretic losses suggest the presence of strong slip inside the gap, facilitating in- and out-flow of ions in the gap. An increase of the tail size reduces the friction force in our model. Depending on the tail size, the friction force decreases with increasing gap for small tails and it increases for large tails.

## 6 Conclusion

Understanding the interplay between the different processes taking place in thin lubricant films is important due to the conflicting demands imposed on how IL lubricants should behave in dynamic confinement. On the one hand, a high load-carrying capability requires strong adsorption of the lubricant to the surface, while, on the other hand, fast self-healing and low friction require high mobility/low viscosity. Our results confirm that the behaviour of ILs in confinement can be unrelated to their bulk behaviour, and therefore, it should be possible to achieve simultaneously, typically conflicting, low friction and good anti-wear performance. A search for optimal IL lubricants, using either synthesis and test methods or state-of-the-art computer-aided molecular design methods,<sup>42</sup> should take into account the micro-scale properties of lubricating thin films (*e.g.*, normal force *vs.* number of layers characteristics), in which the effects of molecular-level processes are more pronounced. Directing the optimisation efforts towards the micro-scale would enable a better differentiation of the qualities of different ionic liquids.

## Conflicts of interest

There are no conflicts to declare.

## Acknowledgements

M. D. and I. S. acknowledge the support of the Ministry of Education, Science and Technological Development of the Republic of Serbia under Project No. OI171017 and the support of COST Action MP1303. All computer simulations were performed on the PARADOX supercomputing facility at the Scientific Computing Laboratory of the Institute of Physics Belgrade, University of Belgrade, Serbia.

## References

- 1 F. Zhou, Y. Liang and W. Liu, *Chem. Soc. Rev.*, 2009, **38**, 2590–2599.
- 2 R. Hayes, G. G. Warr and R. Atkin, *Phys. Chem. Chem. Phys.*, 2010, **12**, 1709–1723.
- 3 C. Dold, T. Amann and A. Kailer, *Lubr. Sci.*, 2013, **4**, 251–268.
- 4 W. Liu, C. Ye, Y. Chen, Z. Ou and D. Sun, *Tribol. Int.*, 2002, **35**, 503–509.
- 5 A. Pensado, M. Comunas and J. Fernández, *Tribol. Lett.*, 2008, **31**, 107–118.
- 6 I. Minami, *Molecules*, 2009, **14**, 2286–2305.
- 7 I. Bou-Malham and L. Bureau, *Soft Matter*, 2010, **6**, 4062–4065.
- 8 D. A. Beattie, R. M. Espinosa-Marzal, T. T. Ho, M. N. Popescu, J. Ralston, C. J. Richard, P. M. Sellapperumage and M. Krasowska, *J. Phys. Chem. C*, 2013, **117**, 23676–23684.
- 9 Z. Wang and C. Priest, *Langmuir*, 2013, **29**, 11344–11353.
- 10 A. M. Smith, K. R. Lovelock, N. N. Gosvami, T. Welton and S. Perkin, *Phys. Chem. Chem. Phys.*, 2013, **15**, 15317–15320.
- 11 A. E. Somers, P. C. Howlett, D. R. MacFarlane and M. Forsyth, *Lubricants*, 2013, **1**, 3.
- 12 B. Bhushan, J. N. Israelachvili and U. Landman, *Nature*, 1995, **374**, 607–616.
- 13 H. Kamimura, T. Chiba, T. Kubo, H. Nanao, I. Minami and S. Mori, *Jpn. J. Tribol.*, 2006, **51**, 675–687.
- 14 S. Perkin, L. Crowhurst, H. Niedermeyer, T. Welton, A. M. Smith and N. N. Gosvami, *Chem. Commun.*, 2011, **47**, 6572–6574.
- 15 H. Wang, Q. Lu, C. Ye, W. Liu and Z. Cui, *Wear*, 2004, **256**, 44–48.
- 16 A. Jiménez, M. Bermudez, P. Iglesias, F. Carrión and G. Martínez-Nicolás, *Wear*, 2006, **260**, 766–782.
- 17 Z. Mu, F. Zhou, S. Zhang, Y. Liang and W. Liu, *Tribol. Int.*, 2005, **38**, 725–731.
- 18 K. Gkagkas, V. Ponnuchamy, M. Dašić and I. Stanković, *Tribol. Int.*, 2017, **113**, 83–91.
- 19 N. Voeltzel, A. Giuliani, N. Fillot, P. Vergne and L. Joly, *Phys. Chem. Chem. Phys.*, 2015, **17**, 23226–23235.
- 20 A. C. F. Mendonça, A. A. H. Pádua and P. Malfreyt, *J. Chem. Theory Comput.*, 2013, **9**, 1600–1610.
- 21 F. Federici Canova, H. Matsubara, M. Mizukami, K. Kurihara and A. L. Shluger, *Phys. Chem. Chem. Phys.*, 2014, **16**, 8247–8256.
- 22 O. Y. Fajardo, F. Bresme, A. A. Kornyshev and M. Urbakh, *J. Phys. Lett.*, 2015, **6**, 3998–4004.
- 23 O. Y. Fajardo, F. Bresme, A. A. Kornyshev and M. Urbakh, *Sci. Rep.*, 2015, **5**, 7698 EP.
- 24 R. Capozza, A. Vanossi, A. Benassi and E. Tosatti, *J. Chem. Phys.*, 2015, **142**, 064707.
- 25 J. Gao, W. D. Luedtke, D. Gourdon, M. Ruths, J. N. Israelachvili and U. Landman, *J. Phys. Chem. B*, 2004, **108**, 3410–3425.
- 26 M. O. Robbins and M. H. Müser, in *Modern Tribology Handbook, Two Volume Set*, ed. B. Bhushan, CRC Press, 2000.
- 27 R. E. Rudd and J. Q. Broughton, *Phys. Rev. B: Condens. Matter Mater. Phys.*, 1998, **58**, R5893–R5896.
- 28 Y. Wang, W. Jiang, T. Yan and G. A. Voth, *Acc. Chem. Res.*, 2007, **40**, 1193–1199.
- 29 D. M. Heyes, E. R. Smith, D. Dini, H. A. Spikes and T. A. Zaki, *J. Chem. Phys.*, 2012, **136**, 134705.
- 30 C. Gattinoni, D. M. Heyes, C. D. Lorenz and D. Dini, *Phys. Rev. E: Stat., Nonlinear, Soft Matter Phys.*, 2013, **88**, 052406.
- 31 L. Martinie and P. Vergne, *Tribol. Lett.*, 2016, **63**, 21.
- 32 M. Dašić, I. Stanković and K. Gkagkas, *Eur. Phys. J. E: Soft Matter Biol. Phys.*, 2018, **41**, 130.
- 33 S. Plimpton, *J. Comput. Phys.*, 1995, **117**, 1–19.
- 34 R. Hayes, G. G. Warr and R. Atkin, *Chem. Rev.*, 2015, **115**, 6357–6426.
- 35 D. J. Evans and G. Morriss, *Phys. Rev. A: At., Mol., Opt. Phys.*, 1984, **30**, 1528.

- 36 P. J. Daivis and B. Todd, *J. Chem. Phys.*, 2006, **124**, 194103.
- 37 M. S. Green, *J. Chem. Phys.*, 1954, **22**, 398–413.
- 38 R. Kubo, *J. Phys. Soc. Jpn.*, 1957, **12**, 570–586.
- 39 S. Perkin, *Phys. Chem. Chem. Phys.*, 2012, **14**, 5052–5062.
- 40 R. Hayes, N. Borisenko, M. K. Tam, P. C. Howlett, F. Endres and R. Atkin, *J. Phys. Chem. C*, 2011, **115**, 6855–6863.
- 41 S. Bair, L. Martinie and P. Vergne, *Tribol. Lett.*, 2016, **63**, 37.
- 42 K. Padiuszyński and U. Domańska, *J. Chem. Inf. Model.*, 2014, **54**, 1311–1324.